A computational approach for characterizing the structural basis of intrinsic coupling modes of the cerebral cortex

Arnaud Messé[1*], Lena J. Meinert[1], Karl J. Hollensteiner[2], Céline Delettre[1], Leigh-Anne Dell[1], Florian Pieper[2], Benoit Larrat[3], Sébastien Meriaux[3], Jean-François Mangin[3], Isabel Reillo[4], Camino de Juan Romero[4], Víctor Borrell[4], Roberto Toro[5,6], Gerhard Engler[2], Andreas K. Engel[2], Claus C. Hilgetag[1,7]

1 Institute of Computational Neuroscience, University Medical Center Hamburg-Eppendorf, Hamburg University, Hamburg, Germany
2 Department of Neurophysiology and Pathophysiology, University Medical Center Hamburg-Eppendorf, Hamburg University, Hamburg, Germany
3 NeuroSpin, CEA, Paris-Saclay University, Gif-sur-Yvette, France
4 Developmental Neurobiology Unit, Instituto de Neurociencias, Consejo Superior de Investigaciones Científicas - Universidad Miguel Hernández, Sant Joan d'Alacant, Spain
5 Unité de Génétique Humaine et Fonctions Cognitives, Département de Neuroscience, Institut Pasteur, Paris, France
6 Center for Research and Interdisciplinarity (CRI), Université Paris Descartes, Paris, France
7 Department of Health Sciences, Boston University, Boston, Massachusetts, USA

* a.messe@uke.de

Abstract

Intrinsic coupling modes (ICMs) reflect the patterns of functional connectivity or synchronization between neuronal ensembles during spontaneous brain activity. These coupling modes represent a widely used concept in modern cognitive neuroscience for probing the connectional organization of intact or damaged brains. However, the principles that shape ICMs remain elusive, in particular their relation to the underlying brain structure. Here we explored ICMs from spontaneous resting awake activity of multiple cortical areas recorded using custom micro-electrocorticographic (μECoG) arrays chronically implanted in ferrets. Additionally, we obtained different kinds of structural connectivity estimates for the regions underlying the ECoG arrays. Then we use large-scale computational models to explore the ability to predict both types of ICMs. Overall, our results reveal that patterns of cortical functional coupling as reflected in phase and envelope ICMs are strongly related to the underlying structural connectivity, to the extent that simple computational models based on the SC topology already reproduce the functional coupling patterns reasonably well.

Introduction

Intrinsic coupling modes (ICMs) reflect the patterns of functional connectivity or synchronization between neuronal ensembles during spontaneous brain activity [1]. These coupling modes represent a widely used concept in modern cognitive neuroscience for probing the connectional organization of intact or damaged brains.

ICM variability has been associated with individual characteristics such as behavior and cognitive abilities [2–5], and aberrant ICM patterns have been linked to a variety of brain diseases [6–8]. However, the principles that shape ICMs remain elusive. This concerns in particular their relation to the underlying brain structure [9]. Therefore, a careful investigation of the relation of ICMs to structural connectivity is required in order to advance our understanding of the network basis of cognition and behavior [9–13].

Numerous studies in animals and humans have suggested that ICMs occur across a broad range of spatial and temporal scales, involving two distinct types of dynamics, namely phase ICMs (pICMs) and envelope ICMs (eICMs) [1]. Phase ICMs involve ongoing oscillatory signals with band-limited dynamics, which can be quantified by measures of phase coupling and which typically occur at frequencies between about 1 Hz and 150 Hz. By contrast, envelope ICMs correspond to coupled slow fluctuations, typically on time scales of a few seconds to minutes, which can be uncovered by the correlation of signal envelopes or signal power. In general, ICMs can be studied with a broad variety of invasive and non-invasive methods, ranging from single-cell recordings to functional MRI. A widely used approach is the analysis of resting-state fMRI functional connectivity (FC), based on signal correlations [14]. Using neurophysiological approaches, such as MEG, EEG, LFP or spike recordings, it becomes possible to study ICMs across a broad range of temporal and spatial scales, in a spectrally resolved manner [11, 15–17]. The available data suggest that phase and envelope ICMs may reflect the operation of distinct coupling mechanisms [1].

One of the main ingredient of the emergence of synchronized activity is the underlying brain structure, specifically, structural connectivity (SC) between brain regions. In this context, diffusion MRI has transformed the field by its ability to estimate the whole brain architecture of structural connections in a non-invasive manner [18]. While pioneer studies have demonstrated a tight association between the patterns of structural and fMRI-based functional connectivity [19–22], the mechanisms underlying the two types of ICMs and their relation to SC are only partly resolved. MRI-based structural connectivity remains controversial and subject to debates regarding its ability to reliably map the actual anatomical connectivity of the brain. On the one hand, it has been shown that tractography incurs a number of biases which result in a substantial number of false positive findings [23–25]. But on the other hand, tractography estimates appear fairly well correlated with tract-tracing findings [26, 27]. In any case, the impact of such biases in the context of computational modeling studies is still unknown.

Large-scale biophysical models have offered mathematical tools for explicitly linking SC to ICMs [10, 28]. In particular, extensive modeling has focused on the relation of eICMs to the underlying SC. Most connectivity-based computational models presented in recent years have in fact focused on describing regional interactions at slow time scales. A variety of models have been developed for this purpose that specifically consider the influence of parameters such as structural weights, delays and noise on neural dynamics [10]. In addition, it has been shown that such slow intrinsic interactions are strongly shaped by the characteristic structural connectivity of the brain [29]. Remarkably, substantially different computational models of the local network nodes can result in similar FC patterns [30, 31]. Candidates for such similarities may include the underlying topology of brain networks as well as a potential degeneracy of the measures defining FC [32]. Much less well understood are interactions at faster time scales, i.e., phase ICMs, and their relations to the underlying anatomy. Nonetheless, a few studies have reported that pICMs appear also to be related to SC [33, 34].

Against this background, the current study set out to pursue three hypotheses.

First, we hypothesized that envelope and phase ICMs are related to SC in a complementary way depending on the frequency. Particularly, we presumed that phase ICMs are more close to SC for high frequencies, while envelope ICMs should show the opposite. Second, it is generally expected that the best match to empirical ICM data can be achieved by using biologically realistic models. And finally, we expected that computational models combined with ground-truth structural connectivity data, as retrieved from retrograde tracer injections, should have more predictive power compared to when used with SC estimates from diffusion MRI tractography.

To test these hypotheses, spontaneous resting awake activity of multiple cortical areas was recorded using custom micro-electrocorticographic (μECoG) arrays chronically implanted in ferrets (*Mustela putorius furo*). The resulting recordings reflect the brain's intrinsic functional network organization. Additionally, we obtained different kinds of structural connectivity estimates for the regions underlying the ECoG arrays. Then we use large-scale computational models to explore the ability to predict both types of ICMs (Fig 1). Overall, our results reveal that patterns of cortical functional coupling as reflected in phase and envelope ICMs are strongly related to the underlying structural connectivity, to the extent that simple computational models based on the SC topology already reproduce the functional coupling patterns reasonably well.

Results

Structure-function relationship

Contrary to our first hypothesis, phase and envelope ICMs were related to SC in a similar way, and thus independent of specific frequency bands (Fig 2). Generally, we observed a positive correlation between ICMs and SC, which slightly increased with frequency.

Predicting intrinsic coupling modes

We employed two computational models with different complexity: the spiking attractor network (SAN) model, a biologically realistic model of a large networks of spiking neurons, and the spatial autoregressive (SAR) model, a statistical model capturing the stationary behavior of a diffuse process on networks. In general, the computational models predicted ICMs better than SC alone. Contrary to our second hypothesis, the simple SAR model outperformed the predictions of empirical ICMs compared to the SAN model (Figs 3 and 4). Distance as a measure of goodness of fit appeared to be more sensitive and appropriate compared to the classic measure of correlation, because there exists no clear coupling strength values that maximized the correlation between empirical and simulated ICMs and coupling strength values with maximal correlations generally led to patterns of simulated ICMs distant from the empirical ones.

For the SAN model, the predictions appeared more nuanced depending on the measure (distance or correlation) and the frequency (Fig 3). Regarding the SAR model, we observed stable predictive values across frequencies with a significant reduction of the distance to ICMs compared to SC and an only slight increases in correlation (Fig 4). Compared to the SAN model, the SAR model had a clear predictive peak depending on the coupling strength.

Influence of the sources of structural data

While diffusion MRI tractography is the only non-invasive approach able to map whole-brain structural connectivity, one may wonder how its limitations (such as lack of directionality) and potential biases (false positives) may affect the predictive ability of connectivity-based computational models. When we compared the predictive power of the SAR model on the basis of different kinds of structural connectivity, only very subtle differences appeared (Fig 5). All three sources of anatomical data gave rise to similar results, which is partly expected given that they are also to some extent inter-correlated. While we cannot distinguish the anatomical data in terms of distance between simulated and empirical ICMs, more pronounced differences appeared for the correlation beween simulated and empirical ICMs. Here, SC based on diffusion MRI tractography and tract-tracing data had similar and higher predictive power than structural connectivity data derived by homology relations from cat connectivity.

Discussion

In the present study, we investigated the relationship between structural connectivity and intrinsic coupling modes in the ferret brain. We also explored and compared the performance of two connectivity-based computational models of very different complexity in modeling envelope and phase ICMs. Finally, we compared the predictive performance of the models for different kinds of underlying structural connectivity data. Generally, we found that SC was strongly related to the ICMs and that a basic autoregressive model best matched the empirical data. Overall, our results suggest that phase and envelope ICMs during spontaneous awake brain activity largely reflect the anatomical organization of cortical networks.

In previous studies, envelope ICMs and their association with structural connectivity were mainly investigated using fMRI data, where consistent positive correlations between SC and eICMs were reported [19–22]. Some recent studies have extended and confirmed these analyzes based on the refined temporal resolution offered by MEG recordings [28, 35]. The relationship between phase ICMs and structural connectivity has been explored using both EEG [33, 34, 36] and MEG [37, 38] data. Similar as for eICMs, a positive relationship between pICMs and SC has been reported consistently, but its potential frequency dependence has not yet been thoroughly investigated. Here, we confirm these observations by showing that both eICMs and pICMs are strongly correlated to SC. As a matter of fact, both measures (eICMs and pICMs) appeared strongly correlated to each other independent of frequency. To the best of our knowledge, the present study is the first that simultaneously explored phase and envelope ICMs from the same dataset.

Using computational models of very different complexity we showed the potential of the models for predicting both kinds of ICMs. Surprisingly, a basic model of a diffuse stationary process appeared to best capture essential ICM patterns.

Moreover, we showed that different kinds of structural connectivity data provided very similar performance in terms of predicting empirical ICMs. The structural connectivity data that we used had different origins and composition (weighted undirected connectivity for diffusion MRI tractography, versus weighted directed connectivity for histological tract-tracing data, versus ordinal directed connectivity derived by homology relations from cat connectivity data). Nonetheless, they have moderate correlations between each other, which may explain their similar predictive performance.

The present results are subject to several important methodological considerations. First and foremost, despite a concept being widely adopted, brain connectivity (both

structural and functional) is under massive investigations and debates on the best approaches for obtaining proper estimates and on their interpretations. While the issues related to SC has been already described above, ICM remains a concept largely elusive given its vague definition and a lack of clear interpretations [32]. We here employed classic and widely used measures of coherence and power correlation as a proxy for phase and envelope ICMs, respectively. While there is an abundant literature which has provided meaningful insights into brain architecture using this measure, it would be informative to see whether alternative definitions nuance the structure-function relationship. Regarding computational modeling, we make use of standard models together with theirs default settings (except for the coupling strength). For further refinement, it could be considered to optimize a larger number of parameters or even to incorporate knowledge from external modalities including, for example, receptor maps [39] or microscopic anatomical (laminar) details [40].

Materials and methods

Intrinsic coupling modes

Intrinsic coupling modes were extracted from μECoG recordings of ferret brain activity during periods of resting awake state. Five adult female ferrets (*Mustela putorius furo*) were used for experiments (Euroferret, Dybbølsgade, Denmark). Each ferret was kept in a standard ferret cage Type 4541 P by Tecniplast (Hohenpeißberg, Germany) with an enriched environment under controlled ambient conditions (21°, 12-h light/dark cycle, lights on at 8:00 a.m.). The animals had ad libitum access to food pellets and to tap water. All behavioral testing was done during the light cycle between 12 a.m. and 6 p.m. All experiments were approved by the independent Hamburg state authority for animal welfare (BUG Hamburg) and were performed in accordance with the guidelines of the German Animal Protection Law.

μECoG preparation and recording

We employed a μECoG array co-developed with the University of Freiburg (ECoG-array; IMTEK, Freiburg) covering a large portion of the posterior, parietal, and temporal surface of the left ferret brain hemisphere [41]. Sixty-four platinum electrodes ($\varnothing$ 250 μm) were arranged equidistantly (1.5 mm) in a hexagonal manner. Thin-film metallization of electrodes and connection lines was sandwiched between two polyimide layers that served as substrate and insulation. See Fig 1 for a schematic diagram of the μECoG layout.

Animals were initially anesthetized with an injection of a mix of ketamine (15 mg/kg), atropine (0.15 mg/kg) and medetomidine (0.08 mg/kg). Physiological parameters such as the ECG and rectal temperature were monitored throughout the surgery to maintain the state of the animal. To maintain anesthesia, additional ketamine (20 mg/kg) was given after each hour or on demand. All surgical procedures were performed under sterile conditions. After preparing the operating area, a craniotomy was performed over the left posterior cortex. The dura was carefully reflected, and the μECoG array was gently placed on the surface of the cortex such that it covered occipital, temporal and parietal areas (Fig. 1B). The dura was then folded back over the μECoG, and an absorbable artificial dura (Braun, Germany) was placed above the surgical area. The excised piece of bone was fixed back in place with titanium plates and screws, gaps were filled with fast set putty (Synthes, Germany). Finally, the μECoG interface was placed on top of the skull and fixed in place with dental cement. After the surgery the animals received preventive analgesics (carprofen, 4 mg/kg) and antibiotics (enrofloxacin, 5 mg/kg) for 8 days.

After recovery from surgery, ferrets were gradually accustomed to a recording box (45×20×52 cm) that was placed in a dark sound attenuated chamber. Once animals were ready for recordings, they were connected to a counter-balanced recording cable that was sufficiently long to enable them to move freely throughout the entire recording box. To monitor animal movement, an accelerometer was tightly attached to the cable-interface close to the head. Ferrets had no access to food or water during recording sessions. For each animal, we obtained at least 4 separate recording sessions that were longer than 2 hours. μECoG signals were digitized at 1.4 kHz (0.1 Hz high pass and 357 Hz low pass filters), and sampled simultaneously with a 64 channel AlphaLab SnRTM recording system (Alpha Omega Engineering, Israel). We analyzed a total of 23 recording sessions.

For each animal, the position of μECoG arrays over posterior cortex was recorded during surgery by taking photographs through a Zeiss OPMI pico microscope. The position of all 64 μECoG electrodes was then projected onto a scaled illustration of a model ferret brain. The precise position of a reference electrode on the scaled ferret brain was measured, along with the angle required to rotate the μECoG such that all electrodes aligned with the picture from surgery. A rotation matrix was then used to translate the location of all 64 μECoG electrodes onto the standard map of the ferret cortex [42]. The cortical region underlying each electrode was then noted, with regions clustered more generally into occipital, parietal, and temporal brain regions (Fig. 8A).

μECoG analysis

We analyzed μECoG recorded from 5 ferrets with at least 4 separate sessions during spontaneous neuronal activity, in the absence of any explicit task. Throughout each session, the brain displays transient changes in state, as evidenced by shifts in behavior and vigilance. These brain states has been objectively classified into slow-wave sleep, rapid-eye-movement sleep and awake periods, using a data-driven approach [43]. The present study focus only on resting awake periods.

To control for drifting and movement related artifacts the electrodes were average-referenced, the global average signal across the entire μECoG grid was subtracted from each time series. Noise epochs were detected using a threshold of 10 standard deviations. Data were rejected in a window of $\pm$ 10 s from all time points that exceeded this threshold. Then, notch filters were applied to remove line noise and its harmonics (50, 100, and 150 Hz), and the data were downsampled to 700 Hz. All data were visually inspected before further analysis to exclude μECoG or other electrical artifacts. Signals were extracted from periods labelled as resting awake state. Periods shorter than 10 s were discarded to increase statistical power. We obtained on average 34 periods of 78 s per session across animals.

Frequency analysis were performed on 60 logarithmically spaced frequency points from 0.1 to 160 Hz. For each session, phase and envelope ICMs were computed between all pairs of electrodes using the measures of coherence and power correlation, respectively. The coherence represents the analogue of the classic correlation-based FC in fMRI for frequency resolved data. It is a normalized measure of the linear relationship between oscillatory signals, where a high value corresponds to signals with similar amplitude and aligned phases. Fast Fourier transform were computed using a multitaper method based on Hanning windows, and phase ICMs were computed across epochs. The power correlation is a measure of the similarity between the power envelopes of the recorded signals [17, 44, 45]. Analysis of such signal can be used to capture slow fluctuations similar to what is provided by fMRI. Time-resolved spectra were computed by convolving the signal with a series of Morlet wavelets, and envelope ICMs were computed per frequency and averaged across epochs.

To account for inter-animal differences in the position of the μECoG-array and

thus make cross-animal comparisons possible, ICM matrices were calculated at the area-level using the atlas of Bizley et al. [42]. Each electrode was assigned to a cortical area by a 'winner-takes-all' method using the maximum overlap, and the average ICM values between these areas were computed. In total, 13 areas were covered by the μECoG-array for all animals. ICM matrices were also averaged across animals to increase statistical power. Additionally, ICMs were averaged within canonical frequency bands: 0.5-3 Hz (delta); 4-7 Hz (theta); 8-15 Hz (alpha); 16-30 Hz (beta); 30-100 Hz (gamma).

All data analysis was performed using custom scripts for Matlab (Mathworks Inc) and the Fieldtrip software [46].

Structural connectivity

Ferret brain structural connectivity data were based on diverse sources, including diffusion MRI-based tractography, retrograde tract tracing experiments, and from homology with connectivity data from the cat brain. The main results were based on structural connectivity estimated by diffusion MRI tractography covering the 13 areas available from the μECoG recordings. As the retrograde histological tracer experiments only investigated a restricted number of areas (7 in total, namely areas 17, 18, 19, 20, 21, PPc and PPr), the comparison of the different sources of structural connectivity were only done for that subset.

Diffusion MRI tractography

High resolution MRI were acquired *ex vivo* from a 2 month old ferret using a small animal 7 Tesla Bruker MRI scanner (Neurospin, Saclay, France). The ferret was perfused transcardially with phosphate-buffered 4% paraformaldehyde. All procedures were approved by the IACUC of the Universidad Miguel Hernández and CSIC.

T2-weighted scan was acquired using a multi-slice multi echo (MSME) sequence with 18 echo times and 0.12 mm isotropic voxels. Diffusion MRI scan was acquired using the following parameters: TR = 40000 ms; TE = 32 ms; matrix size = 160x120x80; 0.24 mm isotropic voxels; 200 diffusion-weighted directions with b = 4000 s/mm^2; and 10 b0 at the beginning of the sequence. The total acquisition time was about 72 hours.

Diffusion MRI were first visually inspected to exclude volume with artifacts. The preprocessing steps included: local principal component analysis denoising [47], Gibbs ringing correction [48], FSL-based eddy current correction [49, 50] and B1 field inhomogeneity correction [51]. Tractography was performed based on the fiber orientation distribution estimated with a multi-tissue constrained spherical deconvolution (msmt CSD). The response functions were computed using the 'dhollander' algorithm which provides an unsupervised estimation of the white matter, grey matter and cerebrospinal fluid response functions. The msmt CSD were performed using a WM/CSF compartment model [52]. The streamline tractographies were then produced following a probabilistic algorithm (iFOD2). One million streamlines were tracked over the full brain with the parameters recommended by MRtrix3: stepsize 0.12 mm, angle 45^{circ} per voxel, minimal streamline length 1.2 mm, maximal length 2.4 cm. Structural connectivity matrices were computed using the number of streamlines connecting pairs of regions of the Bizley atlas. The matrices were inherently symmetric as diffusion MRI tractography does not provide any information about directionality.

All data analysis was performed using custom scripts for Python (Python Software Foundation; `www.python.org`) and the MRtrix3 software (`http://www.mrtrix.org/`).

Retrograde tracer

Structural connectivity data from anatomical tract-tracing experiments on adult ferrets (2 years old) were obtained from [53–55]. The experiments examined the cortico-cortical and cortico-thalamic connectivity of areas 17, 18, 19 and 21 (occipital visual cortex), 20a and 20b (temporal visual cortex), PPc and PPr (posterior parietal visual cortex) in adult ferrets by means of retrograde BDA tracer. Refer to [53–55] for further details of the experimental procedures.

Cat homology

Given similar genetic profile [56] and analogous brain structures, i.e., sulci and gyri [57, 58], it is supposed that cats (*Felis catus*) and ferrets would also share comparable connectional architectures. Thus, we use this homology to map the structural connections, which have been extensively studies in the cat [59], into the ferret. Most areas from the Bizley atlas have an homologue in the cat brain. Areas SSY corresponds to areas PMLS (posterior medial lateral suprasylvian) and VLS (ventricular lateral suprasylvian) in the cat; area PPc to area 7; area PPr to areas 5am, 5al, 5bm and 5bl; and area SIII to areas 1 and 2.

Computational models

We employed two computational models of different complexity. The SAN model, a biologically realistic model of a large networks of spiking neurons [60], and the SAR model, a basic statistical model capturing the stationary behavior of a diffuse process on networks [61]. All models had a parameter that represents the coupling strength between regions. This parameter was optimized separately for each model, see Statistics section. Structural connectivity matrices were normalized before simulations such that the matrices rows sum to one [30, 62].

SAN model

The SAN model is a detailed computational model based on spiking neurons and realistic synapses. A description for the microscopic level, that is within areas, is achieved by using a biologically realistic model of interconnected populations of excitatory and inhibitory neurons. The postsynaptic activity is dependent on the incoming synaptic input currents from other neurons through AMPA, NMDA and GABA receptors, as well as from external background input modeled by Poisson spike trains. Excitatory populations are interconnected at large-scale (inter-areas) *via* the structural connectivity scaled by a global coupling strength factor. For a detailed description refer to [10]

We explored coupling parameter values from 0.1 to 10 by step of 0.1. For each coupling strength value, the SAN model was simulated at a sampling frequency of 10 kHz for 5 minutes. The resulting data were then downsampled to 1 kHz. Simulated ICMs from the neuronal activity were extracted from a similar way as for the empirical data. Phase ICMs were computed by extracting epochs of 10s.

SAR model

The SAR model assumes that fluctuating neuronal signals (y) are related through a model of structural equations, which model relies on expressing each signal as a linear function of the others, weighted by a global coupling strength factor ω, leading to a model

$$y = \omega D y + e, \tag{1}$$

where D represents the structural connectivity matrix and e the input noise. According to Eq 1, y is multivariate normal with covariance

$$(I - \omega D)^{-1} \sigma^2 (I - \omega D')^{-1}, \tag{2}$$

where I stands for the identity matrix, σ^2 the variance of the noise, and $'$ is the regular matrix transposition.

We explored coupling parameter values from 0.001 to 0.999 by step of 0.02. The SAR model provides a closed form for the covariance matrix that can be used to directly compute the predicted ICMs *via* its normalization. Of note, the stationary SAR model does not provide frequency-resolved ICMs, but assumes a common pattern across frquencies.

Statistics

In order to probe structure-function relationships as well as the predictive power of the different models, we computed Pearson correlations as well as distances, that is, the root-mean-square deviation, between SC, simulated and empirical ICM matrices. Diagonal elements of matrices were excluded to avoid spurious variations of the prediction. Additionally, when exploring structure-function relationships, SC was spectrally normalized (divided by its maximal eigen-value), to avoid offsets of the distance measure due to different scales.

Coupling strength values were selected according to the predictive power measures by either maximizing or minimizing the distance the correlation between simulated and empirical ICMs. Importantly, coupling strengths were optimized separately for phase and envelope ICMs.

Acknowledgments

This work was supported by grants from the Deutsche Forschungsgemeinschaft (DFG): SFB936/A1/A2/Z3, SPP1665/EN533/13-1 and SPP2041/HI1286/6-1/EN533/15-1. The funders had no role in study design, data collection and analysis, decision to publish, or preparation of the manuscript.

References

1. Engel AK, Gerloff C, Hilgetag CC, Nolte G. Intrinsic Coupling Modes: Multiscale Interactions in Ongoing Brain Activity. Neuron. 2013;80(4):867–886. doi:10.1016/j.neuron.2013.09.038.

2. Fries P. A mechanism for cognitive dynamics: neuronal communication through neuronal coherence. Trends in Cognitive Sciences. 2005;9:474–80.

3. Fox M, Raichle ME. Spontaneous fluctuations in brain activity observed with functional magnetic resonance imaging. Nature Reviews Neuroscience. 2007;8:700–11. doi:10.1038/nrn2201.

4. Hipp JF, Engel AK, Siegel M. Oscillatory Synchronization in Large-Scale Cortical Networks Predicts Perception. Neuron. 2011;69(2):387–396. doi:10.1016/j.neuron.2010.12.027.

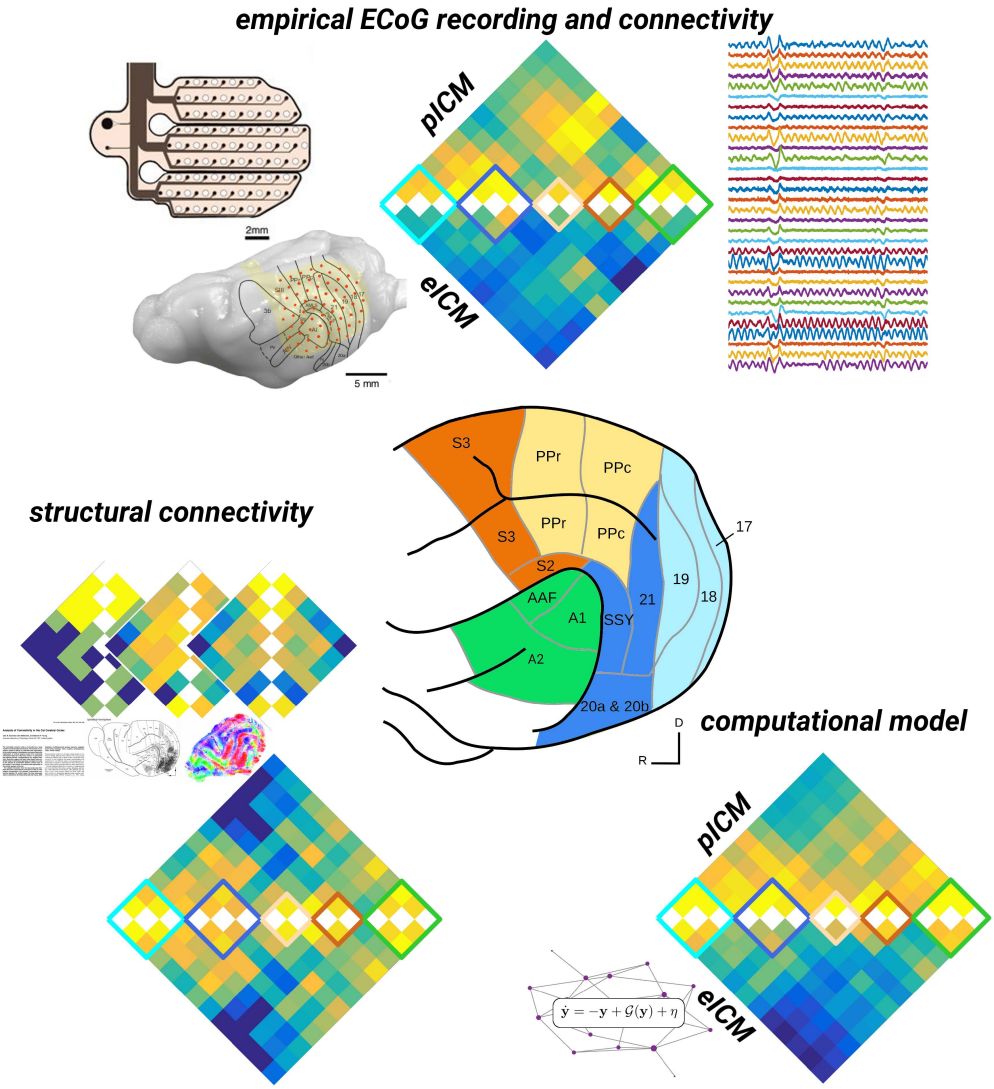

Fig 1. Multimodal processing pipeline. (A) Empirical μECoG recording and ICMs. Design and example of the placement over the left posterior ferret cortex. The μECoG consists of 64 platinum electrodes distributed across three polymide fingers to enable the array to adapt to the curved surface of the cortex. From the resulting brain activity signals, phase and envelope ICMs were computed and mapped to the parcellation of the ferret cerebral cortex by Bizley et al. [42]. (B) Ferret cortex parcellated into 13 functionally and anatomically distinct regions according to [42]. Abbreviations: LS: lateral sulcus; SSS: suprasylvian sulcus; A: anterior; P: posterior; M: medial; L: lateral; S2/S3: somatosensory cortex 2 & 3; PPr/c: rostral/caudal posterior parietal cortex; 17,18,19,20,21: occipital/visual cortex; SSY: suprasylvian field; A1/A2: primary and secondary auditory cortex; AAF: anterior auditory field. (C) Patterns of structural connectivity from diverse anatomical sources (Cat homology, tract-tracing, and diffusion MRI tractography. (D) Large-scale computational brain models. Example of simulated phase and envelope ICMs.

5. Smith S, Nichols T, Vidaurre D, Winkler A, Behrens T, Glasser M, et al. Nature Neuroscience. 2015;18(11):1565–1567. doi:10.1038/nn.4125.

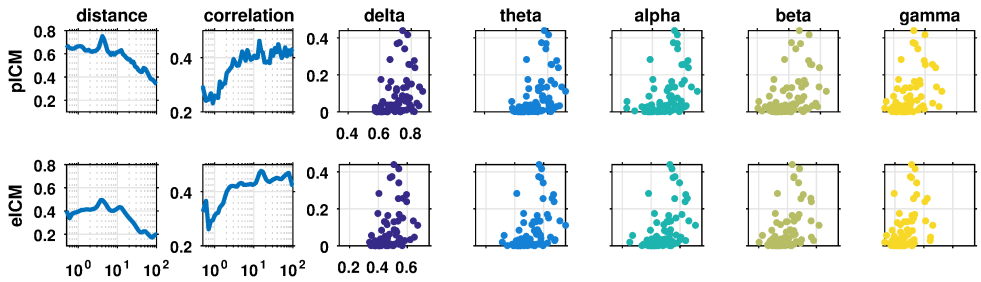

Fig 2. Structure-function relationship. (A) Distance and correlation of structural connectivity with phase and envelope ICMs as a function of the carrier frequency. (B) Scatter plots of ICMs versus SC across canonical frequency bands.

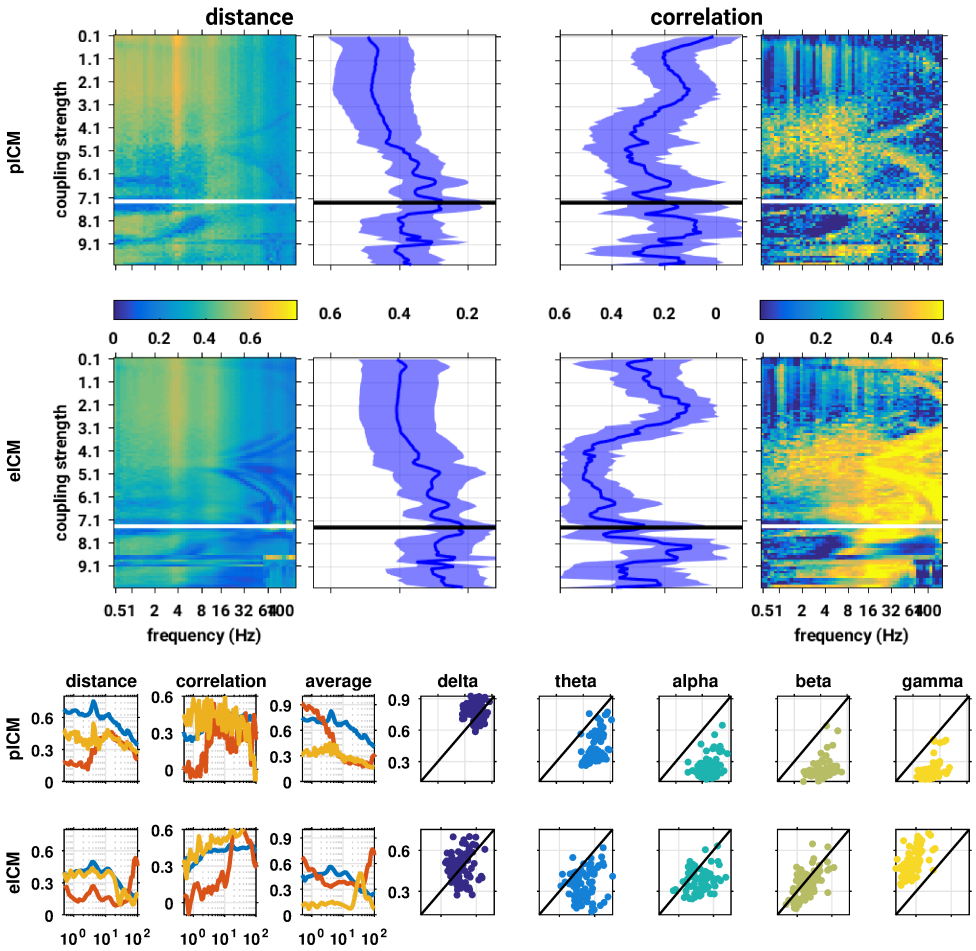

Fig 3. Predictive power of the SAN model. (A) Parameter space exploration. (B) Distance, correlation and averaged values of the simulated ICMs with the empirical ones as a function of the carrier frequency. Blue, red and orange curve represent the values from the structural connectivity, the simulated ICMs minimizing the distance and maximizing the correlation, respectively. (C) Scatter plots of empirical versus simulated ICMs which minimize distance, across canonical frequency bands (solid line represents the identity).

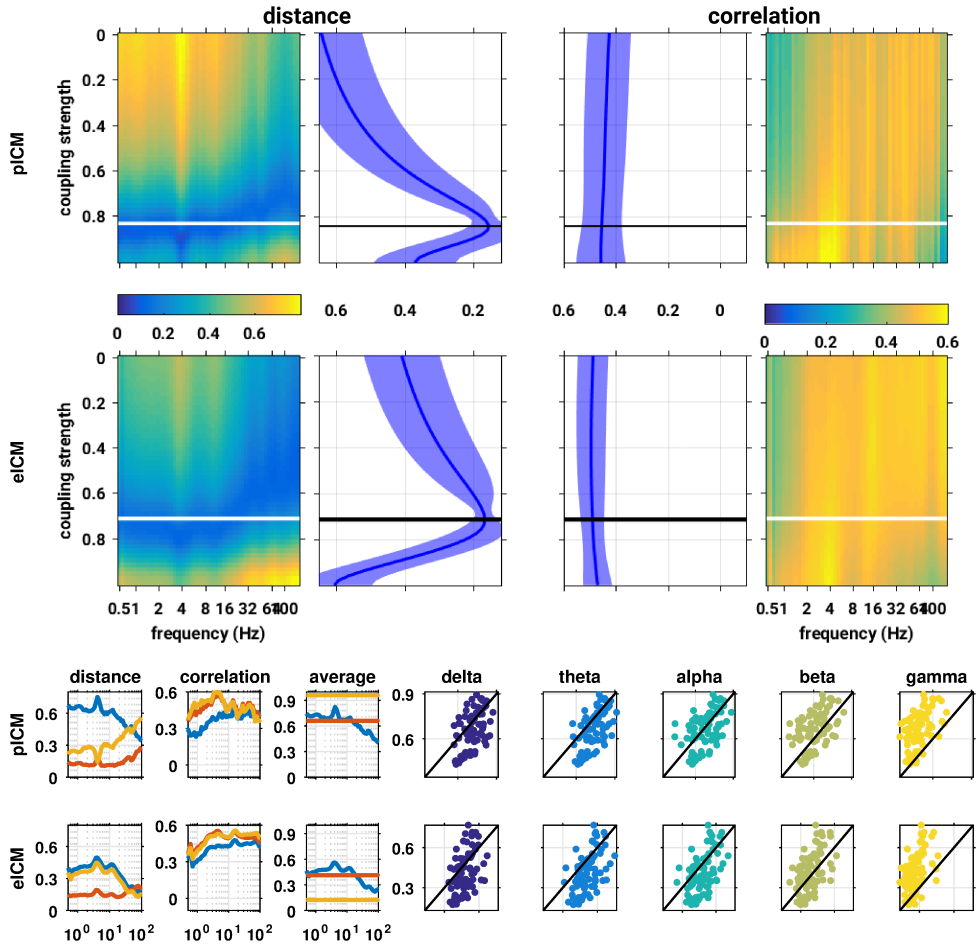

Fig 4. Predictive power of the SAR model. (A) Parameter space exploration. (B) Distance, correlation and averaged values of the simulated ICMs with the empirical ones as a function of the carrier frequency. Blue, red and orange curve represent the values from the structural connectivity, the simulated ICMs minimizing the distance and maximizing the correlation, respectively. (C) Scatter plots of empirical versus simulated ICMs which minimize distance, across canonical frequency bands (solid line represents the identity).

6. Schnitzler A, Gross J. Normal and pathological oscillatory communication in the brain. Nature Reviews Neuroscience. 2005;6(4):285–296. doi:10.1038/nrn1650.

7. Uhlhaas P, Singer W. Neuronal Dynamics and Neuropsychiatric Disorders: Toward a Translational Paradigm for Dysfunctional Large-Scale Networks. Neuron. 2012;75(6):963–980. doi:10.1016/j.neuron.2012.09.004.

8. Fornito A, Bullmore ET. Connectomics: A new paradigm for understanding brain disease. European Neuropsychopharmacology. 2015;25(5):733–748. doi:10.1016/j.euroneuro.2014.02.011.

9. Park HJ, Friston K. Structural and Functional Brain Networks: From Connections to Cognition. Science. 2013;342(6158):1238411. doi:10.1126/science.1238411.

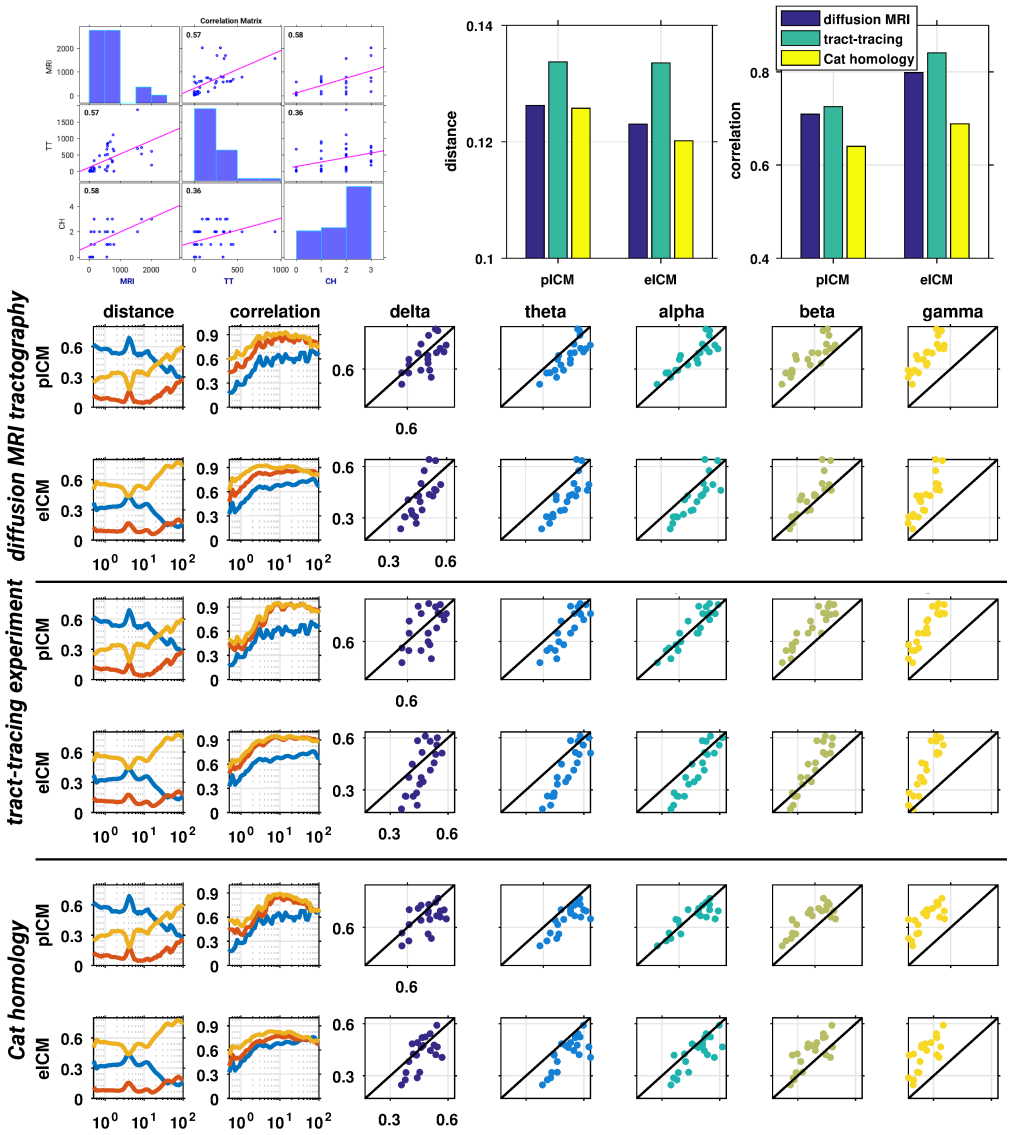

Fig 5. Predictive power of the SAR model using different source of anatomical data. (A) Parameter space exploration. (B) Distance, correlation and averaged values of the simulated ICMs with the empirical ones as a function of the carrier frequency. Blue, red and orange curve represent the values from the structural connectivity, the simulated ICMs minimizing the distance and maximizing the correlation, respectively. (C) Scatter plots of empirical versus simulated ICMs which minimize distance, across canonical frequency bands (solid line represents the identity).

10. Deco G, Jirsa V, McIntosh A. Emerging concepts for the dynamical organization of resting-state activity in the brain. Nature Reviews Neuroscience. 2011;12:43–56. doi:10.1038/nrn2961.

11. Siegel M, Donner T, Engel A. Spectral fingerprints of large-scale neuronal interactions. Nat Rev Neurosci. 2012;13(2):121–134. doi:10.1038/nrn3137.

12. Singer W. Cortical dynamics revisited. Trends in Cognitive Sciences. 2013;17:616–626.

13. Sporns O. Contributions and challenges for network models in cognitive neuroscience. Nature neuroscience. 2014;17(5):652–660.

14. Raichle M. Two views of brain function. Trends in Cognitive Sciences. 2010;14:180–90. doi:10.1016/j.tics.2010.01.008.

15. Lachaux JP, Rodriguez E, Martinerie J, Varela FJ. Measuring phase synchrony in brain signals. Human Brain Mapping;8(4):194–208. doi:10.1002/(SICI)1097-0193(1999)8:4¡194::AID-HBM4¿3.0.CO;2-C.

16. Nolte G, Bai O, Wheaton L, Mari Z, Vorbach S, Hallett M. Identifying true brain interaction from EEG data using the imaginary part of coherency. Clinical Neurophysiology. 2004;115(10):2292–2307. doi:10.1016/j.clinph.2004.04.029.

17. Hipp JF, Hawellek DJ, Corbetta M, Siegel M, Engel AK. Large-scale cortical correlation structure of spontaneous oscillatory activity. Nature Neuroscience. 2012;15:884–90.

18. Le Bihan D, Heidi JB. Diffusion MRI at 25: exploring brain tissue structure and function. NeuroImage. 2011;61(2):324–341. doi:10.1016/j.neuroimage.2011.11.006.

19. Koch MA, Norris DG, Hund-Georgiadis M. An Investigation of Functional and Anatomical Connectivity Using Magnetic Resonance Imaging. NeuroImage. 2002;16(1):241–250. doi:10.1006/nimg.2001.1052.

20. Vincent JL, Patel GH, Fox MD, Snyder AZ, Baker JT, Van Essen DC, et al. Intrinsic functional architecture in the anaesthetized monkey brain. Nature. 2007;447:83–6. doi:10.1038/nature05758.

21. Hagmann P, Cammoun L, Gigandet X, Meuli R, Honey C, Wedeen V, et al. Mapping the structural core of human cerebral cortex. PLoS Biology. 2008;6:e159. doi:10.1371/journal.pbio.0060159.

22. Greicius MD, Supekar K, Menon V, Dougherty RF. Resting-state functional connectivity reflects structural connectivity in the default mode network. Cerebral Cortex. 2009;19:72–78. doi:10.1093/cercor/bhn059.

23. Thomas C, Ye F, Irfanoglu O, Modi P, Saleem K, Leopold D, et al. Anatomical accuracy of brain connections derived from diffusion MRI tractography is inherently limited. Proceedings of the National Academy of Sciences of the USA. 2014;111(46):16574–16579. doi:10.1073/pnas.1405672111.

24. Reveley C, Seth A, Pierpaoli C, Silva A, Yu D, Saunders R, et al. Superficial white matter fiber systems impede detection of long-range cortical connections in diffusion MR tractography. Proceedings of the National Academy of Sciences of the USA. 2015;112(21).

25. Maier-Hein KH, Neher PF, Houde C, Côté MA, Garyfallidis E, Zhong J, et al. The challenge of mapping the human connectome based on diffusion tractography. Nature Communications. 2017;8(1). doi:10.1038/s41467-017-01285-x.

26. Calabrese E, Badea A, Cofer G, Qi Y, Johnson GA. A Diffusion MRI Tractography Connectome of the Mouse Brain and Comparison with Neuronal Tracer Data. Cerebral Cortex. 2015;doi:10.1093/cercor/bhv121.

27. Donahue CJ, Sotiropoulos SN, Jbabdi S, Hernandez-Fernandez M, Behrens TE, Dyrby TB, et al. Using Diffusion Tractography to Predict Cortical Connection Strength and Distance: A Quantitative Comparison with Tracers in the Monkey. Journal of Neuroscience. 2016;36(25):6758–6770. doi:10.1523/JNEUROSCI.0493-16.2016.

28. Joana C, Morten L K, Gustavo D. Exploring the network dynamics underlying brain activity at rest. Progress in Neurobiology. 2014;114:102–31.

29. Goñi J, van den Heuvel MP, Avena-Koenigsberger A, Velez de Mendizabal N, Betzel RF, Griffa A, et al. Resting-brain functional connectivity predicted by analytic measures of network communication. Proceedings of the National Academy of Sciences of the USA. 2014;111(2):833–838. doi:10.1073/pnas.1315529111.

30. Messé A, Rudrauf D, Benali H, Marrelec G. Relating Structure and Function in the Human Brain: Relative Contributions of Anatomy, Stationary Dynamics, and Non-Stationarities. PLoS Computational Biology. 2014;10:e1003530.

31. Messé A, Rudrauf D, Giron A, Marrelec G. Predicting functional connectivity from structural connectivity via computational models using MRI: An extensive comparison study. NeuroImage. 2015;111C:65–75.

32. Marrelec G, Messé A, Giron A, Rudrauf D. Functional Connectivity's Degenerate View of Brain Computation. PLoS Computational Biology. 2016;12(10):e1005031.

33. Chu CJ, Tanaka N, Diaz J, Edlow BL, Wu O, H$\hat{\text{"}}$am$\hat{\text{"}}$aläinen M, et al. EEG functional connectivity is partially predicted by underlying white matter connectivity. NeuroImage. 2015;108:23–33. doi:10.1016/j.neuroimage.2014.12.033.

34. Finger H, Bönstrup M, Cheng B, Messé A, Hilgetag C, Thomalla G, et al. Modeling of Large-Scale Functional Brain Networks Based on Structural Connectivity from DTI: Comparison with EEG Derived Phase Coupling Networks and Evaluation of Alternative Methods along the Modeling Path. PLoS Computational Biology. 2016;12(8):e1005025. doi:10.1371/journal.pcbi.1005025.

35. Garcés P, Pereda E, Hernàndez-Tamames JA, Del-Pozo F, Maestù F, Ángel Pineda-Pardo J. Multimodal description of whole brain connectivity: A comparison of resting state MEG, fMRI, and DWI. Human Brain Mapping. 2016;37(1):20–34. doi:10.1002/hbm.22995.

36. Wirsich J, Ridley B, Besson P, Jirsa V, Bénar C, Ranjeva JP, et al. Complementary contributions of concurrent EEG and fMRI connectivity for predicting structural connectivity. NeuroImage. 2017;161:251–260. doi:10.1016/j.neuroimage.2017.08.055.

37. Tewarie P, Hillebrand A, van Dellen E, Schoonheim MM, Barkhof F, Polman CH, et al. Structural degree predicts functional network connectivity: A multimodal resting-state fMRI and MEG study. NeuroImage. 2014;97:296–307. doi:10.1016/j.neuroimage.2014.04.038.

38. Meier J, Tewarie P, Hillebrand A, Douw L, van Dijk BW, Stufflebeam SM, et al. A Mapping Between Structural and Functional Brain Networks. Brain Connectivity. 2016;6(4):298–311. doi:10.1089/brain.2015.0408.

39. Deco G, Cruzat J, Cabral J, Knudsen GM, Carhart-Harris RL, Whybrow PC, et al. Whole-Brain Multimodal Neuroimaging Model Using Serotonin Receptor Maps Explains Non-linear Functional Effects of LSD. Current biology. 2018;28:3065–3074. doi:10.1016/j.cub.2018.07.083.

40. Schmidt M, Bakker R, Shen K, Bezgin G, Diesmann M, van Albada SJ. A multi-scale layer-resolved spiking network model of resting-state dynamics in macaque visual cortical areas. PLoS Computational Biology. 2018;14(10):1–38. doi:10.1371/journal.pcbi.1006359.

41. Rubehn B, Bosman C, Oostenveld R, Fries P, Stieglitz T. A MEMS-based flexible multichannel ECoG-electrode array. Journal of Neural Engineering. 2009;6(3):036003. doi:10.1088/1741-2560/6/3/036003.

42. Bizley JK, Nodal FR, Bajo VM, Nelken I, King AJ. Physiological and Anatomical Evidence for Multisensory Interactions in Auditory Cortex. Cerebral Cortex. 2007;17(9):2172–2189. doi:10.1093/cercor/bhl128.

43. Stitt I, Hollensteiner KJ, Galindo-Leon E, Pieper F, Fiedler E, Stieglitz T, et al. Dynamic reconfiguration of cortical functional connectivity across brain states. Scientific reports. 2017;7:8797. doi:10.1038/s41598-017-08050-6.

44. Brookes MJ, Woolrich M, Luckhoo H, Price D, Hale JR, Stephenson MC, et al. Investigating the electrophysiological basis of resting state networks using magnetoencephalography. Proceedings of the National Academy of Sciences of the USA. 2011;108:16783–8.

45. de Pasquale F, Della Penna S, Snyder A, Marzetti L, Pizzella V, Romani G, et al. A Cortical Core for Dynamic Integration of Functional Networks in the Resting Human Brain. Neuron. 2012;74(4):753–764. doi:10.1016/j.neuron.2012.03.031.

46. Oostenveld R, Fries P, Maris E, Schoffelen JM. FieldTrip: Open source software for advanced analysis of MEG, EEG, and invasive electrophysiological data. Computational intelligence and neuroscience. 2011;2011:156869. doi:10.1155/2011/156869.

47. Veraart J, Novikov DS, Christiaens D, Ades-aron B, Sijbers J, Fieremans E. Denoising of diffusion MRI using random matrix theory. NI. 2016;142:394–406. doi:10.1016/j.neuroimage.2016.08.016.

48. Kellner E, Dhital B, Kiselev VG, Reisert M. Gibbs-ringing artifact removal based on local subvoxel-shifts. Magnetic Resonance in Medicine. 2016;76(5):1574–1581. doi:10.1002/mrm.26054.

49. Jenkinson M, Beckmann CF, Behrens TEJ, Woolrich MW, Smith SM. FSL. NeuroImage. 2012;62:782–90.

50. Andersson JLR, Sotiropoulos SN. An integrated approach to correction for off-resonance effects and subject movement in diffusion MR imaging. NeuroImage. 2016;125:1063–1078. doi:10.1016/j.neuroimage.2015.10.019.

51. Tustison NJ, Avants BB, Cook PA, Zheng Y, Egan A, Yushkevich PA, et al. N4ITK: Improved N3 Bias Correction. IEEE Transactions on Medical Imaging. 2010;29(6):1310–1320. doi:10.1109/TMI.2010.2046908.

52. Jeurissen B, Tournier JD, Dhollander T, Connelly A, Sijbers J. Multi-tissue constrained spherical deconvolution for improved analysis of multi-shell diffusion MRI data. NI. 2014;103:411 – 426. doi:10.1016/j.neuroimage.2014.07.061.

53. Dell LA, Innocenti GM, Hilgetag CC, Manger PR. Cortical and thalamic connectivity of occipital visual cortical areas 17, 18, 19 and 21 of the domestic ferret (Mustela putorius furo). in revision;doi:10.1101/491399.

54. Dell LA, Innocenti GM, Hilgetag CC, Manger PR. Cortical and thalamic connectivity of temporal visual cortical areas 20a and 20b of the domestic ferret (Mustela putorius furo). in revision;doi:10.1101/492728.

55. Dell LA, Innocenti GM, Hilgetag CC, Manger PR. Cortical and thalamic connectivity of posterior parietal visual cortical areas PPc and PPr of the domestic ferret (Mustela putorius furo). in revision;doi:10.1101/491993.

56. Cavagna P, Menotti A, Stanyon R. Genomic homology of the domestic ferret with cats and humans. Mammalian Genome. 2000;11:886–870. doi:0.1007/s003350010172.

57. Manger PR, Nakamura H, Valentiniene S, Innocenti GM. Visual Areas in the Lateral Temporal Cortex of the Ferret (Mustela putorius). Cerebral Cortex. 2004;14(6):676–689. doi:10.1093/cercor/bhh028.

58. Foxworthy WA, Meredith MA. An examination of somatosensory area SIII in ferret cortex. Somatosensory & Motor Research. 2011;28(1-2):1–10. doi:10.3109/08990220.2010.548465.

59. Scannell J, Blakemore C, Young M. Analysis of connectivity in the cat cerebral cortex. Journal of Neuroscience. 1995;15(2):1463–1483. doi:10.1523/JNEUROSCI.15-02-01463.1995.

60. Deco G, Jirsa VK. Ongoing cortical activity at rest: Criticality, multistability, and ghost attractors. The Journal of Neuroscience. 2012;32:3366–75.

61. Messé A, Benali H, Marrelec G. Relating structural and functional connectivity in MRI: A simple model for a complex brain. IEEE Transactions on Medical Imaging. 2015;34:27–37. doi:10.1109/TMI.2014.2341732.

62. Cabral J, Hugues E, Sporns O, Deco G. Role of local network oscillations in resting-state functional connectivity. NeuroImage. 2011;57:130–9. doi:10.1016/j.neuroimage.2011.04.010.